Materials Horizons

ROYAL SOCIETY OF CHEMISTRY

COMMUNICATION

View Article Online
View Journal

Cite this: DOI: 10.1039/d4mh01105h

Received 19th August 2024,
Accepted 10th September 2024

DOI: 10.1039/d4mh01105h

rsc.li/materials-horizons

Tuning the circularly polarized phosphorescence of platinum(II) complexes through a chiral cation strategy†

Jiajia Ren,‡[a] Tengfei He,‡[ad] Haolin Lu,[a] Hebin Wang,[a] Tianyin Shao,[a] Zhaoyu Wang,[a] Yunxin Zhang,[a] Sehrish Gull,[a] Yun Chi,[b] Yu-Wu Zhong,[c] Yongsheng Chen[d] and Guankui Long*[a]

Circularly polarized phosphorescent (CPP) materials, especially chiral platinum(II) complexes, which combine the advantages of both circularly polarized luminescence (CPL) and phosphorescence, show broad potential applications in chiral optoelectronic devices. Developing CPP emitters with both excellent chiroptical properties and high yield is urgently needed. Here, a chiral cation strategy is employed to construct the CPP Pt(II) complexes *R*/*S*-ABA·[Pt(ppy)Cl$_2$] and *R*/*S*-MBA·[Pt(ppy)Cl$_2$] through a simple one-step reaction with almost 100% yield. The circular dichroism and CPL spectra confirm that the chirality was successfully transferred to the [Pt(ppy)Cl$_2$]$^-$ anion. The luminescence asymmetry factors (g_{lum}) are +1.4/−1.8 × 10^{-3} for *R*/*S*-ABA·[Pt(ppy)Cl$_2$] and +4.4/−2.8 × 10^{-3} for *R*/*S*-MBA·[Pt(ppy)Cl$_2$]. The stronger chiroptical property of *R*/*S*-MBA·[Pt(ppy)Cl$_2$] is attributed to the enhanced chiral structural deformation and better matched electric and magnetic transition dipole moments. This chiral cation strategy is confirmed to efficiently construct CPP Pt(II) complexes, which will accelerate the development of CPP emitters towards commercialization.

New concepts

Circularly polarized phosphorescent (CPP) materials show broad potential applications, but generally entail complicated synthesis or difficult enantio-separation using chiral high-performance liquid chromatography. In this work, for the first time, we have proposed a chiral cation strategy and constructed the chiral ionic Pt(II) phosphorescent complexes *R*/*S*-ABA·[Pt(ppy)Cl$_2$] and *R*/*S*-MBA·[Pt(ppy)Cl$_2$] with high yields of nearly 100%. Under the chiral induction effect of the *R*/*S*-ABA$^+$ and *R*/*S*-MBA$^+$ cations, the [Pt(ppy)Cl$_2$]$^-$ anions present significant chiral structural deformation and crystallize into the chiral space groups. The circular dichroism and circularly polarized luminescence spectra further confirm that chirality is successfully transferred to the luminescence center of [Pt(ppy)Cl$_2$]$^-$. The luminescence asymmetry factor (g_{lum}) reaches +1.4/−1.8 × 10^{-3} for *R*/*S*-ABA·[Pt(ppy)Cl$_2$] and +4.4/−2.8 × 10^{-3} for *R*/*S*-MBA·[Pt(ppy)Cl$_2$]. Our work provides an efficient strategy to construct CPP materials with both excellent CPL performance and high yield, which will accelerate the development of these materials towards commercialization.

Introduction

Circular polarized phosphorescent (CPP) materials have attracted wide research interest owing to their combined advantages of both circularly polarized luminescence (CPL) and phosphorescence,[1–3] and have shown fantastic merits in a wide range of applications including encrypted transmission,[4] information storage,[5] and chiroptical switches.[6] In addition to a few examples of pure organic molecules,[7] strong spin–orbit coupling (SOC) effects involving heavy atoms like Pt,[8–10] Ir,[11] Ru,[12] and halogen atoms in complexes could effectively promote intersystem crossing (ISC) to make full use of the singlet and triplet excitons towards highly efficient phosphorescence. Notably, the d^8 configuration Pt(II) complexes have many advantages, such as distinctive molecular packing and tunable photophysical properties, and have thus emerged as promising phosphorescent candidates.[13–17] Conventionally, combining Pt(II) centers with chiral characteristics such as circularly polarized phosphorescent luminescence (CPPL) can be achieved by introducing chiral ligands, such as helicene,[18] 1,1′-binaphthyl,[19] [2.2]paracyclophane,[20] *etc.*[21] However, these

[a] *Tianjin Key Lab for Rare Earth Materials and Applications, Renewable Energy Conversion and Storage Center (RECAST), Smart Sensing Interdisciplinary Science Center, School of Materials Science and Engineering, Nankai University, Tianjin 300350, China. E-mail: longgk09@nankai.edu.cn*

[b] *Department of Materials Science and Engineering, Department of Chemistry, Center of Super-Diamond and Advanced Films (COSDAF), City University of Hong Kong, Hong Kong SAR 999077, China*

[c] *CAS Key Laboratory of Photochemistry, Institute of Chemistry, Chinese Academy of Sciences, Beijing 100190, China*

[d] *The Centre of Nanoscale Science and Technology and State Key Laboratory of Elemento-Organic Chemistry, Frontiers Science Center for New Organic Matter, College of Chemistry, Nankai University, Tianjin 300071, China*

† Electronic supplementary information (ESI) available. CCDC 2365460–2365467. For ESI and crystallographic data in CIF or other electronic format see DOI: https://doi.org/10.1039/d4mh01105h

‡ These authors contributed equally to this work.

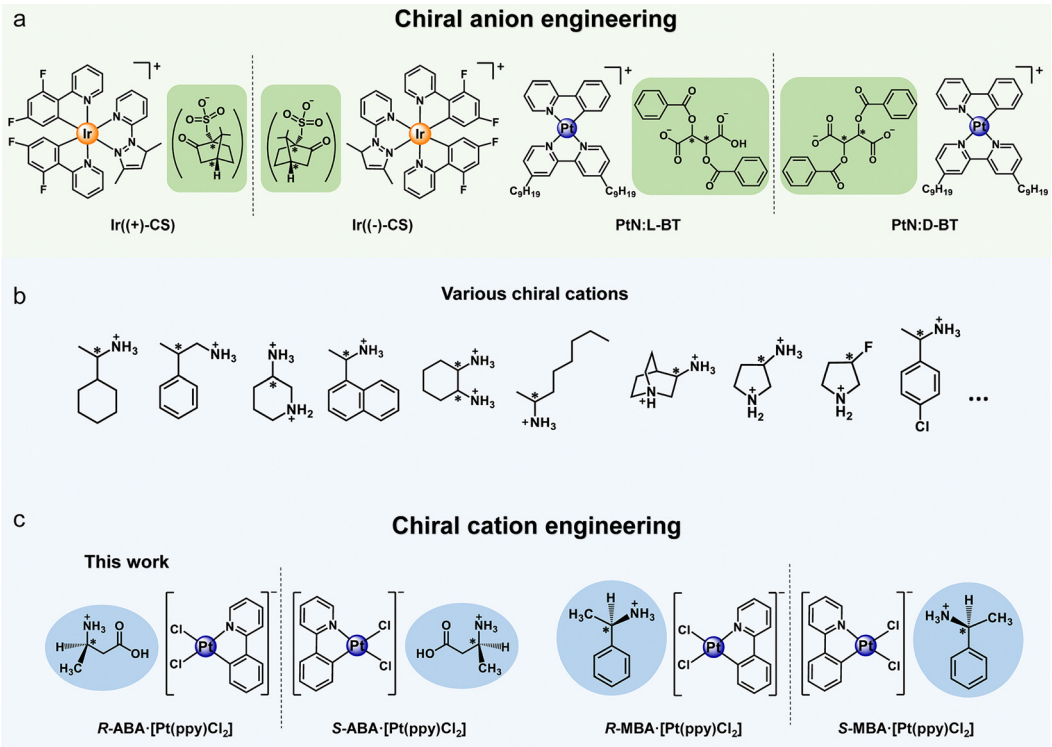

Fig. 1 Chiral anion and chiral cation strategies. (a) Structural formulae of Ir(III) and Pt(II) complexes investigated using the chiral anion strategy. (b) Various chiral cations. (c) Structural formulae of *R*/*S*-ABA·[Pt(ppy)Cl_2] and *R*/*S*-MBA·[Pt(ppy)Cl_2] in this work.

approaches generally entail complicated synthesis or difficult enantioseparation using chiral high-performance liquid chromatography (HPLC); thus it is difficult and expensive to obtain enantiomers on the gram scale,[22–24] which significantly hinders the development and application of CPP materials towards real applications. Therefore, obtaining CPP materials with simple synthesis, low cost, high yield and excellent chiroptical performance remains a major challenge.

Among the continuous attempts, chirality transfer within ionic species was recently proved to be an effective strategy for constructing CPL-emitting materials composed of cationic Pt(II), Ir(III), Ru(II) and Au(I) complexes and chiral anions.[25–28] Zhong *et al.*[25] reported a simple and general chiral anion strategy to prepare CPL-active ionic transition metal complexes through the introduction of (±)-camphorsulfonate ((±)-CS) counter anions as the chiral source into Ir(III) and Ru(II) complexes (Fig. 1(a)). Similarly, You *et al.*[27] integrated the chiral L-/D-dibenzoyl tartarate (L-/D-BT) anion with Pt(2-phenylpyridinato)(4,4′-bis(nonyl)-2,2′-bipyridine) ([PtN]$^+$), and achieved an amplified luminescence dissymmetry factor (g_{lum}) through helical assembly. However, similar exploration of chiral cation-induced transition metal complexes is rarely reported. On the other hand, chiral hybrid organic–inorganic metal halides (HOIMHs) which have the advantages of facile synthesis, good solution processability and excellent photophysical properties, are widely investigated,[29–31] and their chiroptical properties can be successfully tuned by regulating the A-site chiral organic cations.[32–34] Most importantly, compared to the more complicated structure of chiral anions, many more choices of chiral cations are available (as summarized in Fig. 1(b)).[35] Inspired by the success of the chiral anion strategy for transition metal complexes and the widely used chiral cations in chiral HOIMHs, a chiral cation strategy is proposed to simplify the complicated synthesis and tune the molecular packings and chiroptical properties of Pt(II) complexes in this work.

Herein, we report two pairs of chiral anionic Pt(II) complexes, *R*/*S*-ABA·[Pt(ppy)Cl_2] (ABA = 3-aminobutyric acid, ppy = 2-phenylpyridine) and *R*/*S*-MBA·[Pt(ppy)Cl_2] (MBA = methylbenzylamine) with high yields of nearly 100% (Fig. 1(c)). *R*/*S*-ABA·[Pt(ppy)Cl_2] and *R*/*S*-MBA·[Pt(ppy)Cl_2] crystallized into the *Sohncke* space groups $P2_1$ and $P2_12_12_1$, respectively. The equivalent atomic displacement parameters and solid-state NMR measurements revealed that *R*/*S*-MBA·[Pt(ppy)Cl_2] presents a relatively looser packing mode. This space-allowed structural relaxation of *R*/*S*-MBA·[Pt(ppy)Cl_2] leads to temperature-dependent nonradiative transition despite its intrinsic smaller reorganization energy between the ground and triplet excited state. Therefore, *R*/*S*-MBA·[Pt(ppy)Cl_2] exhibits a much lower photoluminescence quantum yield (PLQY) of 13.3% at room temperature and a higher PLQY of 57.7% at 80 K. Circular dichroism (CD) and CPPL measurements confirm that the luminescent center of [Pt(ppy)Cl_2]$^-$ is successfully induced by the chiral cations. The absorption asymmetry factors (g_{abs}) of *R*/*S*-ABA·[Pt(ppy)Cl_2] and *R*/*S*-MBA·[Pt(ppy)Cl_2] were $+1.1/-1.1 \times 10^{-4}$ and $+1.6/-2.0 \times 10^{-3}$, respectively, while the g_{lum} was $+1.4/-1.8 \times 10^{-3}$ for *R*/*S*-ABA·[Pt(ppy)Cl_2] and $+4.4/-2.8 \times 10^{-3}$ for *R*/*S*-MBA·[Pt(ppy)Cl_2]. The stronger chiroptical properties of *R*/*S*-MBA·[Pt(ppy)Cl_2] are attributed to the significant chiral structural

deformation and better matched electric and magnetic transition dipole moments. Our work demonstrates a new and simplified strategy to obtain circularly polarized phosphorescent materials and improve their performance toward CPL light sources.

Results and discussion

Powder samples of *R*/*S*-ABA·[Pt(ppy)Cl_2] and *R*/*S*-MBA·[Pt(ppy)Cl_2] were successfully synthesized by simply mixing [Pt(ppy)(μ-Cl)]$_2$ with chiral *R*/*S*-ABA·Cl or *R*/*S*-MBA·Cl in chloroform. The yields of these one-step reactions can reach up to ~100%. In contrast, for traditional chiral Pt(II) complexes, enormous efforts have been made to acquire efficient chiral structures, and their synthesis typically requires three or more steps and elaborate control over the reaction and purification conditions.[36,37] Single crystals of *R*/*S*-ABA·[Pt(ppy)Cl_2] and *R*/*S*-MBA·[Pt(ppy)Cl_2] were obtained after slow volatilization in methanol at room temperature (RT). The structures of the *R*/*S*-ABA·[Pt(ppy)Cl_2] and *R*/*S*-MBA·[Pt(ppy)Cl_2] were then determined using single crystal X-ray diffraction (SCXRD). The crystal structures of *R*/*S*-ABA·[Pt(ppy)Cl_2] and *R*/*S*-MBA·[Pt(ppy)Cl_2] are shown in Fig. 2 and Fig. S2, S3 (ESI†), the Pt atom adopts a four-coordinated square-planar geometry, as typically observed for Pt(II) phosphorescent complexes.[38–40] The [Pt(ppy)Cl_2]$^-$ anions are separated by the chiral cations in a layered fashion, and both the adjacent [Pt(ppy)Cl_2]$^-$ anions and ABA^+/MBA^+ cations in each layer are packed in different orientations. The closest measured Pt···Pt distances are 7.668 Å for *R*-ABA·[Pt(ppy)Cl_2] and 6.126 Å for *R*-MBA·[Pt(ppy)Cl_2] (Fig. 2), which are twice as large as the van der Waals radius of the platinum atom [r_w(Pt) = 1.4 Å], indicating that there is no Pt···Pt interaction in the crystals. *R*/*S*-ABA·[Pt(ppy)Cl_2] and *R*/*S*-MBA·[Pt(ppy)Cl_2] crystallized into the $P2_1$ and $P2_12_12_1$ *Sohncke* space groups, respectively. Therefore, *R*/*S*-MBA·[Pt(ppy)Cl_2], which has three two-fold screw axes, is conducive to building a stronger chiral packing. This can be further confirmed by examining the symmetries after removing the chiral cations.[41,42] For the [Pt(ppy)Cl_2]$^-$ framework in *R*/*S*-ABA·[Pt(ppy)Cl_2], the space group tends to be achiral $P2_1/n$, indicating the diminished chiral stacking; while that of *R*/*S*-MBA·[Pt(ppy)Cl_2] remains the $P2_12_12_1$ *Sohncke* space group. This indicates that *R*/*S*-MBA·[Pt(ppy)Cl_2] should exhibit stronger chirality transfer by the MBA^+ (Fig. S4–S6, ESI†) and thus better chiroptical properties than *R*/*S*-ABA·[Pt(ppy)Cl_2]. The powder X-ray diffraction (PXRD) pattern matches very well with that simulated from single crystals, confirming the excellent phase purity of the obtained *R*/*S*-ABA·[Pt(ppy)Cl_2] and *R*/*S*-MBA·[Pt(ppy)Cl_2] powders (Fig. S7, ESI†).

For the investigation of crystal rigidity and molecular packings tuned by chiral cations, we first focused on the spin–lattice relaxation rate (R_1) through solid-state NMR measurements (Fig. S8, ESI†).[43,44] The chiral center atom (C_a) and the terminal methyl carbon (C_b) of the cations were compared, and the relaxation rates of C_a/C_b are 0.109/0.959 s^{-1} and 0.186/1.866 s^{-1} for *R*-ABA·[Pt(ppy)Cl_2] and *R*-MBA·[Pt(ppy)Cl_2], respectively (as shown in Fig. 3(a) and (b)). The smaller relaxation rates in *R*-ABA·[Pt(ppy)Cl_2] should be attributed to its more compact stacking. Then, another

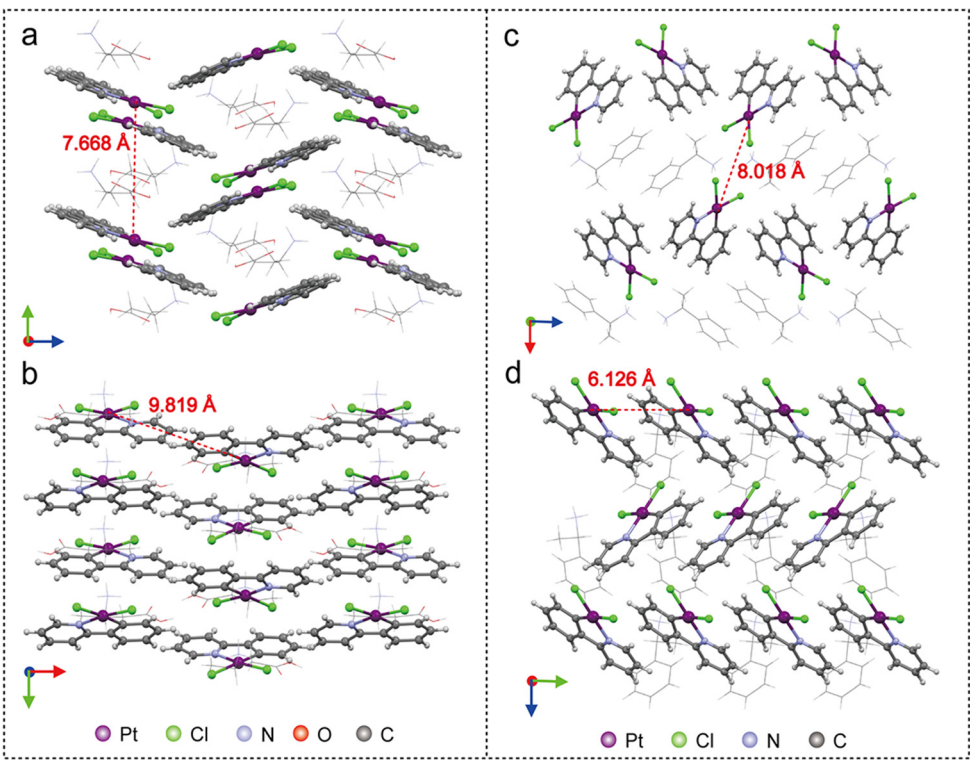

Fig. 2 Crystal structures for *R*-ABA·[Pt(ppy)Cl_2] and *R*-MBA·[Pt(ppy)Cl_2]. (a) and (b) Packing modes in different perspectives and the adjacent Pt···Pt distances for *R*-ABA·[Pt(ppy)Cl_2]. (c) and (d) Packing modes in different perspectives and the adjacent Pt···Pt distances for *R*-MBA·[Pt(ppy)Cl_2].

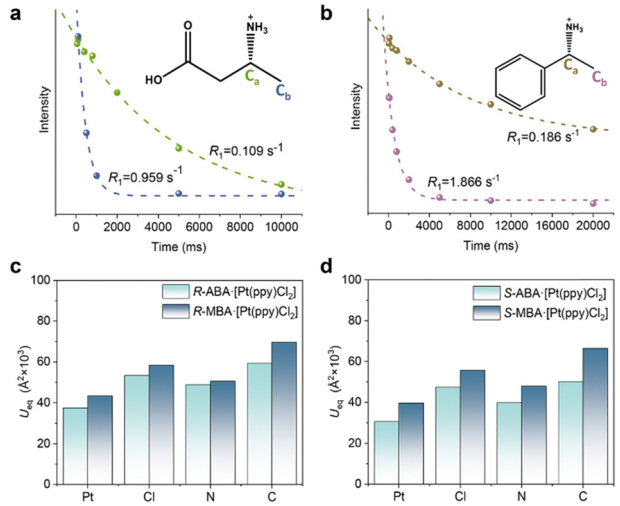

Fig. 3 Spin–lattice relaxation lifetime and atomic displacements of *R*-ABA·[Pt(ppy)Cl$_2$] and *R*-MBA·[Pt(ppy)Cl$_2$]. (a) and (b) Diagrams of the chiral center atom (C$_a$) and the terminal methyl carbon (C$_b$) of the cations, and the fitting of relaxation rates for (a) *R*-ABA·[Pt(ppy)Cl$_2$] and (b) *R*-MBA·[Pt(ppy)Cl$_2$]. (c) and (d) Atomic displacements of the Pt, Cl, N and C atoms for *R*-ABA·[Pt(ppy)Cl$_2$] and *R*-MBA·[Pt(ppy)Cl$_2$] (c) and *S*-ABA·[Pt(ppy)Cl$_2$] and *S*-MBA·[Pt(ppy)Cl$_2$] (d) crystals from SCXRD at 298 K.

indicator of crystal rigidity, the equivalent atomic displacement parameters (U_{eq}), was extracted from the single-crystal structures to further evaluate the overall rigidity of the studied Pt(II) complexes.[45] The U_{eq} of the major atoms in *R*/*S*-ABA·[Pt(ppy)Cl$_2$] present smaller root-mean-squared displacements (Fig. 3(c), (d) and Fig. S9, ESI†), indicating their more rigid structure and restricted relaxation. Additionally, the crystal densities are 3.927 mmol cm^{-3} for *R*-ABA·[Pt(ppy)Cl$_2$] and 3.621 mmol cm^{-3} for *R*-MBA·[Pt(ppy)Cl$_2$] (Table S1, ESI†), confirming the dense packing regulated by the ABA$^+$.

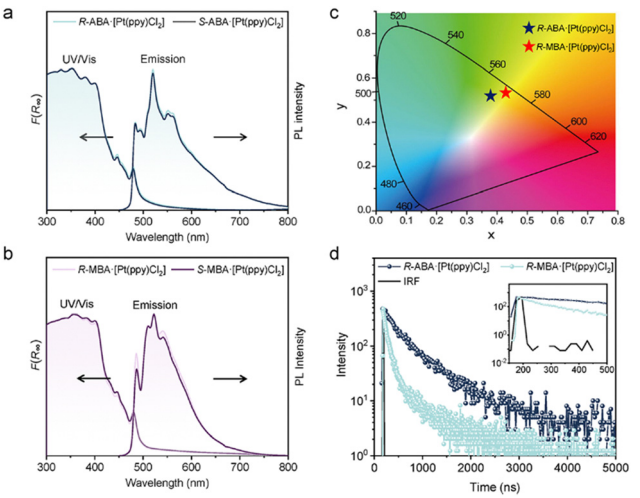

Fig. 4 Photophysical properties of *R*/*S*-ABA·[Pt(ppy)Cl$_2$] and *R*/*S*-MBA·[Pt(ppy)Cl$_2$]. (a), (b) UV/Vis diffuse reflectance and emission spectra (λ_{ex} = 397 nm) of *R*/*S*-ABA·[Pt(ppy)Cl$_2$] (a) and *R*/*S*-MBA·[Pt(ppy)Cl$_2$] (b) powders. (c) CIE chromaticity diagram for the emission spectra of the *R*-ABA·[Pt(ppy)Cl$_2$] and *R*-MBA·[Pt(ppy)Cl$_2$] powders (λ_{ex} = 397 nm) at room temperature. (d) Photoluminescence decay spectra for *R*-ABA·[Pt(ppy)Cl$_2$] and *R*-MBA·[Pt(ppy)Cl$_2$] at room temperature.

These chiral Pt(II) complexes exhibit excellent thermal and air stability. Thermogravimetric analysis shows that weight loss starts at 230 °C for *R*/*S*-ABA·[Pt(ppy)Cl$_2$] and 224 °C for *R*/*S*-MBA·[Pt(ppy)Cl$_2$], which was attributed to the decomposition of organic ABA$^+$ and MBA$^+$ (Fig. S10, ESI†).[46] The *R*/*S*-ABA·[Pt(ppy)Cl$_2$] and *R*/*S*-MBA·[Pt(ppy)Cl$_2$] powders were placed in an air environment, and powder XRD that showed the samples remained stable after eight months (Fig. S11 and S12, ESI†).

The UV-Vis absorption and photoluminescence (PL) spectra of the *R*/*S*-ABA·[Pt(ppy)Cl$_2$] and *R*/*S*-MBA·[Pt(ppy)Cl$_2$] powders were then measured and are shown in Fig. 4(a) and (b). *R*/*S*-ABA·[Pt(ppy)Cl$_2$] displayed almost identical absorption edges to *R*/*S*-MBA·[Pt(ppy)Cl$_2$], indicating that the [Pt(ppy)Cl$_2$]$^-$ ions in *R*/*S*-ABA·[Pt(ppy)Cl$_2$] and *R*/*S*-MBA·[Pt(ppy)Cl$_2$] should behave as "discrete" molecules without Pt···Pt electronic interactions. Therefore, it can be concluded that their electronic and excited state characteristics originate from the coordinated Pt(II) parts rather than the chiral cations.[47–50] This was further confirmed by theoretical calculations. The electronic band structures, total density of states (TDOS) and partial density of states (PDOS) of *R*-ABA·[Pt(ppy)Cl$_2$] and *R*-MBA·[Pt(ppy)Cl$_2$] crystals show that the main contributions to the valence band maximum (VBM) are from the Pt and Cl atoms, while the conduction band minimum (CBM) are almost contributed by the N and C atoms on the ppy ligand (Fig. S13 and S14, ESI†). The chiral cations are not directly involved in the VBM or CBM, or the electronic transitions. Then, detailed absorption spectra were calculated using the quantum mechanics/molecular mechanics (QM/MM) method in the ONIOM model.[51] As summarized in Tables S2, S3 and Fig. S15, S16 (ESI†), the maximum absorption is mainly from the HOMO → LUMO transition, which is a mixture of metal to ligand charge transfer (MLCT), halogen to ligand charge transfer (XLCT) and ligand-centered (LC) [namely, d(Pt) + p(Cl) + π(ppy) → π*(ppy)] transition.

R/*S*-ABA·[Pt(ppy)Cl$_2$] and *R*/*S*-MBA·[Pt(ppy)Cl$_2$] exhibit green and yellow luminescence, respectively (Fig. 4(c) and Fig. S17, ESI†). The maxima of the vibrational satellite band of *R*/*S*-ABA·[Pt(ppy)Cl$_2$] (520 nm) is almost comparable to those of *R*/*S*-MBA·[Pt(ppy)Cl$_2$] (522 nm); the slight red shift of *R*/*S*-MBA·[Pt(ppy)Cl$_2$] might be attributed to the different stacking mode in single crystals (Fig. 2). Through fitting the PL decay spectra, we obtained phosphorescence lifetimes of 0.56/0.57 μs and 0.26/0.30 μs for *R*/*S*-ABA·[Pt(ppy)Cl$_2$] and *R*/*S*-MBA·[Pt(ppy)Cl$_2$] (Fig. 4(d) and Fig. S18, ESI†), respectively.

Photophysical properties are significantly influenced by the intrinsic molecular structure and temperature. The photophysical parameters at room temperature and 80 K are summarized in Table 1. At room temperature, the photoluminescence quantum yields (Φ) are ~19% for *R*/*S*-ABA·[Pt(ppy)Cl$_2$] and ~13% for *R*/*S*-MBA·[Pt(ppy)Cl$_2$]. It is found that the Φ of *R*/*S*-MBA·[Pt(ppy)Cl$_2$] at 80 K increases significantly to ~55%, overtaking that of *R*/*S*-ABA·[Pt(ppy)Cl$_2$] (~34% at 80 K). Then, the temperature-dependent PL spectra were measured, and the spectra became sharper as the temperature decreased (Fig. S19, ESI†).

Table 1 Summary of the photophysical parameters of the Pt(II) complexes

	T [K]	λ_{max} [nm]	τ^a [μs]	Φ [%]	$k_r{}^b$ [s^{-1}]	$k_{nr}{}^c$ [s^{-1}]
R-ABA·[Pt(ppy)Cl_2]	RT	521	0.56	19.9	3.55×10^5	1.43×10^6
	80	497	2.84	34.1	1.20×10^5	2.30×10^5
S-ABA·[Pt(ppy)Cl_2]	RT	520	0.57	19.6	3.44×10^5	1.41×10^6
	80	497	2.47	35.9	2.22×10^5	1.80×10^5
R-MBA·[Pt(ppy)Cl_2]	RT	522	0.26	13.3	5.12×10^5	3.33×10^6
	80	509	1.38	57.7	5.00×10^5	2.25×10^5
S-MBA·[Pt(ppy)Cl_2]	RT	523	0.30	13.2	4.40×10^5	2.89×10^6
	80	509	1.17	54.8	4.68×10^5	3.86×10^5

[a] Emission at λ_{max}. [b] Radiative rate constant, $k_r = \Phi/\tau$. [c] Nonradiative rate constant, $k_{nr} = k_r(1 - \Phi)/\Phi$.

The strengthened emission of the first vibrational satellite band (dashed line, 492 nm in *R*-ABA·[Pt(ppy)Cl_2] and 506 nm in *R*-MBA·[Pt(ppy)Cl_2]) at 80 K indicates the suppressed nonradiative transition (Fig. 5(a) and (b)).

Combined with the corresponding phosphorescence lifetimes, the radiative and nonradiative rate constants (k_r and k_{nr}) can be obtained. It is worth noting that the k_r values of *R*/*S*-ABA·[Pt(ppy)Cl_2] and *R*/*S*-MBA·[Pt(ppy)Cl_2] are similar at both room temperature and low temperature ($>10^5$ s^{-1}), suggesting that the enhancement of Φ at 80 K is due to the decrease of k_{nr} (Table 1), which might result from the suppression of excited state vibrational relaxation. Thus, we calculated the reorganization energy ($\lambda_{T_1 \to S_0}$) to quantify the structural deformation between the lowest triplet excited state (T_1) state and the ground state (S_0). As shown in Fig. 5(c) and (d), the intrinsic $\lambda_{T_1 \to S_0}$ is 0.38 eV for *R*-ABA·[Pt(ppy)Cl_2] and 0.29 eV for *R*-MBA·[Pt(ppy)Cl_2], and the main structural distortions all originated from the vibrations of the ppy ligand. The smaller $\lambda_{T_1 \to S_0}$ of *R*-MBA·[Pt(ppy)Cl_2] indicates its better intrinsic structural rigidity without the disturbance of temperature. The nonradiative transition of *R*-MBA·[Pt(ppy)Cl_2] shows a sensitive dependence on temperature, which might be due to its loose molecular packing in the crystal, which provides space for structural relaxation (Fig. 2 and Fig. S2, S3, ESI†).

The chiroptical properties, such as circular dichroism (CD) and circularly polarized phosphorescence, were then investigated using both experimental measurements and theoretical calculations. As shown in Fig. 6, both *R*/*S*-ABA·[Pt(ppy)Cl_2] and *R*/*S*-MBA·[Pt(ppy)Cl_2] showed perfectly mirrored symmetrical CD spectra together with clear Cotton effects at 328/407 and 335/401 nm, respectively.[52] The experimental and simulated CD spectra are in good agreement. The absorption dissymmetry factors (g_{abs}) were also calculated and are shown in Fig. 6(e) and (f). The maximum g_{abs} of *R*/*S*-ABA·[Pt(ppy)Cl_2] and *R*/*S*-MBA·[Pt(ppy)Cl_2] are $+1.1/-1.1 \times 10^{-4}$ and $+1.6/-2.0 \times 10^{-3}$, respectively. Therefore, it is confirmed that the chirality is successfully transferred to the luminescence center of $[Pt(ppy)Cl_2]^-$ by the chiral cations, and that *R*/*S*-MBA·[Pt(ppy)Cl_2] present stronger chiroptical properties than *R*/*S*-ABA·[Pt(ppy)Cl_2]. In addition to the more stable and pronounced chiral stacking mentioned previously, we further measured the CD spectra of the chiral cations *R*/*S*-ABA·Cl and *R*/*S*-MBA·Cl. The molar ellipticity is

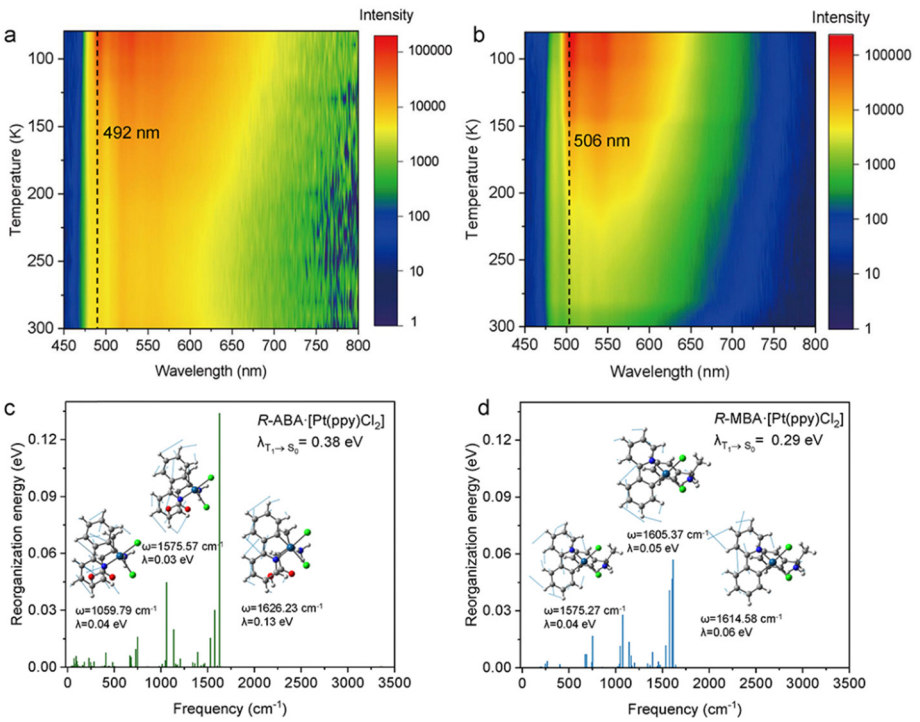

Fig. 5 Temperature-dependent pseudocolor map of the emission spectra and reorganization energy for chiral Pt(II) complexes. (a), (b) Temperature-dependent pseudocolor map of emission spectra and reorganization energy for chiral Pt(II) complexes. Temperature-dependent pseudocolor map of the emission spectra of (a) *R*-ABA·[Pt(ppy)Cl_2] and *R*-MBA·[Pt(ppy)Cl_2] (b). (c), (d) The calculated reorganization energies ($\lambda_{T_1 \to S_0}$) between the S_0 and T_1 states for *R*-ABA·[Pt(ppy)Cl_2] (c) and *R*-MBA·[Pt(ppy)Cl_2] (d); the shift vectors for the normal modes with the top three largest reorganization energies are inserted.

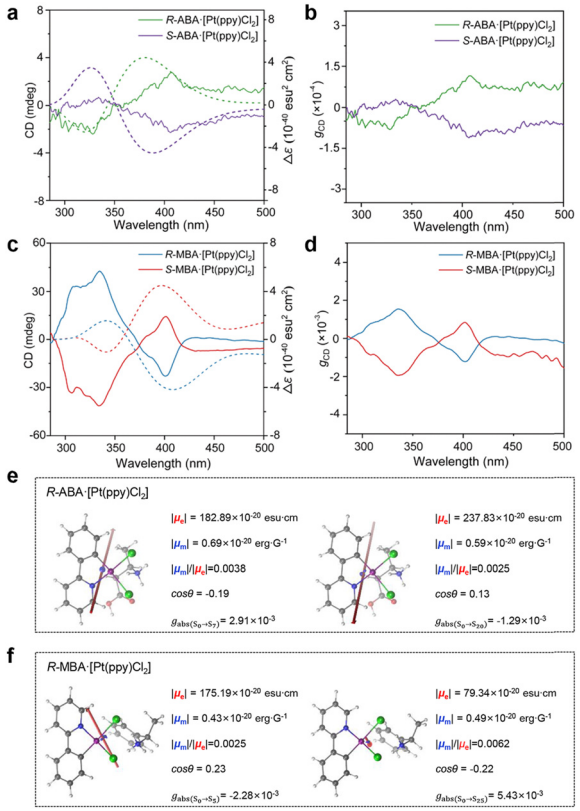

Fig. 6 Chiroptical properties and transition dipole moment analysis. (a), (c) Measured (solid lines) and simulated (dotted lines) CD spectra of *R*/*S*-ABA·[Pt(ppy)Cl$_2$] (a) and *R*/*S*-MBA·[Pt(ppy)Cl$_2$] (c). (b), (d) The corresponding measured g_{abs} spectra of *R*/*S*-ABA·[Pt(ppy)Cl$_2$] (b) and *R*/*S*-MBA·[Pt(ppy)Cl$_2$] (d). (e), (f) The calculated electric transition dipole moment and magnetic transition dipole moment vector analysis of *R*-ABA·[Pt(ppy)Cl$_2$] (e) and *R*-MBA·[Pt(ppy)Cl$_2$] (f) for the main CD peaks.

78.4 deg cm^2 dmol^{-1} for *R*/*S*-ABA·Cl and 94.4 deg cm^2 dmol^{-1} for *R*/*S*-MBA·Cl. This intrinsic stronger circular dichroism of *R*/*S*-MBA·Cl may enable the induced *R*/*S*-MBA·[Pt(ppy)Cl$_2$] complexes to exhibit stronger CD and g_{abs} (Fig. S20, ESI†). Furthermore, g_{abs} can be theoretically calculated based on eqn (1),[53,54]

$$g_{abs} = \frac{4|\mu_e||\mu_m|\cos\theta}{|\mu_e|^2+|\mu_m|^2} \quad (1)$$

in which μ_e and μ_m are the electric and magnetic transition dipole moment vectors, and θ is the angle between these two vectors. When the vectors μ_e and μ_m are equal in length and oriented in either the parallel or antiparallel direction (to maximize $|\cos\theta|$), the absolute value of g_{abs} can reach the maximum value of 2. However, the magnitude of μ_m is typically far smaller than that of μ_e in most chiral molecules, so eqn (1) can be simplified as eqn (2):

$$g_{abs} \approx \frac{4|\mu_m|\cos\theta}{|\mu_e|} \quad (2)$$

Thus, the simplified $|\mu_m|/|\mu_e|$ is always used to quantitatively compare the values of g_{abs}. The electric and magnetic dipole moment vectors for the main CD peaks at around 325–335 nm and 400–410 nm are shown in Fig. 6(e) and (f); the values of $|\mu_m|/|\mu_e|$ and $|\cos\theta|$ of *R*-MBA·[Pt(ppy)Cl$_2$] are both larger than those of *R*-ABA·[Pt(ppy)Cl$_2$], thus contributing to the larger g_{abs} of *R*-MBA·[Pt(ppy)Cl$_2$].

The CPL spectra of *R*/*S*-ABA·[Pt(ppy)Cl$_2$] and *R*/*S*-MBA·[Pt(ppy)Cl$_2$] in poly(methyl methacrylate) (PMMA) were further measured and are shown in Fig. 7. The CPL spectra of *R*- and *S*-ABA·[Pt(ppy)Cl$_2$], and *R*- and *S*-MBA·[Pt(ppy)Cl$_2$] are opposite in the entire emission region, with a g_{lum} of approximately +1.4/-1.8×10^{-3} for *R*/*S*-ABA·[Pt(ppy)Cl$_2$] and +4.4/-2.8×10^{-3} for *R*/*S*-MBA·[Pt(ppy)Cl$_2$], respectively. Just as predicted from the stronger chiral stacking and CD characteristics, a higher g_{lum} is expected in *R*/*S*-MBA·[Pt(ppy)Cl$_2$]. To provide more support, the optimized structures in the emissive T_1 state were compared (Fig. 7(e)). Generally, phosphorescent Pt(II) complexes employ square-planar geometries.[55] When they are induced by chiral sources like MBA$^+$ and ABA$^+$ cations, the chromogenic [Pt(ppy)Cl$_2$]$^-$ presents distorted configurations and enables the unique chiroptical properties. As shown in Fig. 7(e), the dihedral angle between the plane of the ppy ligand (colored in blue) and the plane determined by Pt and two Cl atoms (colored in pink) was employed to illustrate the degree of deformation. It is found that the averaged dihedral angles in the T_1 excited state of [Pt(ppy)Cl$_2$]$^-$ in *R*-ABA·[Pt(ppy)Cl$_2$] and *R*-MBA·[Pt(ppy)Cl$_2$] are 4.50° and 8.60°, respectively. Therefore, *R*-MBA·[Pt(ppy)Cl$_2$] is more influenced by the MBA$^+$ cation and thus has more strengthened chiroptical characteristics in both the single crystal and S_0 state (Fig. S21 and S22, ESI†). Additionally, based on the measured Φ, lifetime and g_{lum}, the values of the electric transition dipole moments ($|\mu_e|$) and magnetic transition dipole moments ($|\mu_m|$) of CPPL for *R*/*S*-ABA·[Pt(ppy)Cl$_2$] and *R*/*S*-MBA·[Pt(ppy)Cl$_2$] can be estimated (collected in Table 2 and Table S8, ESI†). The calculation results show that the $|\mu_m|$ of *R*/*S*-MBA·[Pt(ppy)Cl$_2$] (0.24/0.14 $\times$ 10^{-20}·erg G^{-1}) are greater than those of *R*/*S*-ABA·[Pt(ppy)Cl$_2$] (0.06/0.08 $\times$ 10^{-20}·erg G^{-1}). The increased $|\mu_m|/|\mu_e|$ leads to an enhancement of the CPL strength and larger g_{lum} of the *R*/*S*-MBA·[Pt(ppy)Cl$_2$].

Conclusions

In summary, a chiral cation strategy has been proposed and employed to obtain circularly polarized phosphorescent luminescence based on Pt(II) complexes of *R*/*S*-ABA·[Pt(ppy)Cl$_2$] and *R*/*S*-MBA·[Pt(ppy)Cl$_2$] through a simple one-step reaction with high yields of up to 100%. The *R*/*S*-ABA·[Pt(ppy)Cl$_2$] and *R*/*S*-MBA·[Pt(ppy)Cl$_2$] powders present excellent thermal and air stability. As evidenced by equivalent atomic displacement parameters and solid-state NMR measurement, *R*/*S*-MBA·[Pt(ppy)Cl$_2$] presents a looser packing mode than *R*/*S*-ABA·[Pt(ppy)Cl$_2$]; this space-allowed structural relaxation leads to the temperature-dependent nonradiative transition of *R*/*S*-MBA·[Pt(ppy)Cl$_2$] despite its intrinsic smaller reorganization energy between the S_0 and T_1 states. Therefore, *R*/*S*-MBA·[Pt(ppy)Cl$_2$] exhibits a much lower PLQY of 13.3% at room temperature but a higher PLQY of 57.7% at 80 K. The circular dichroism and circularly polarized phosphorescence spectra of

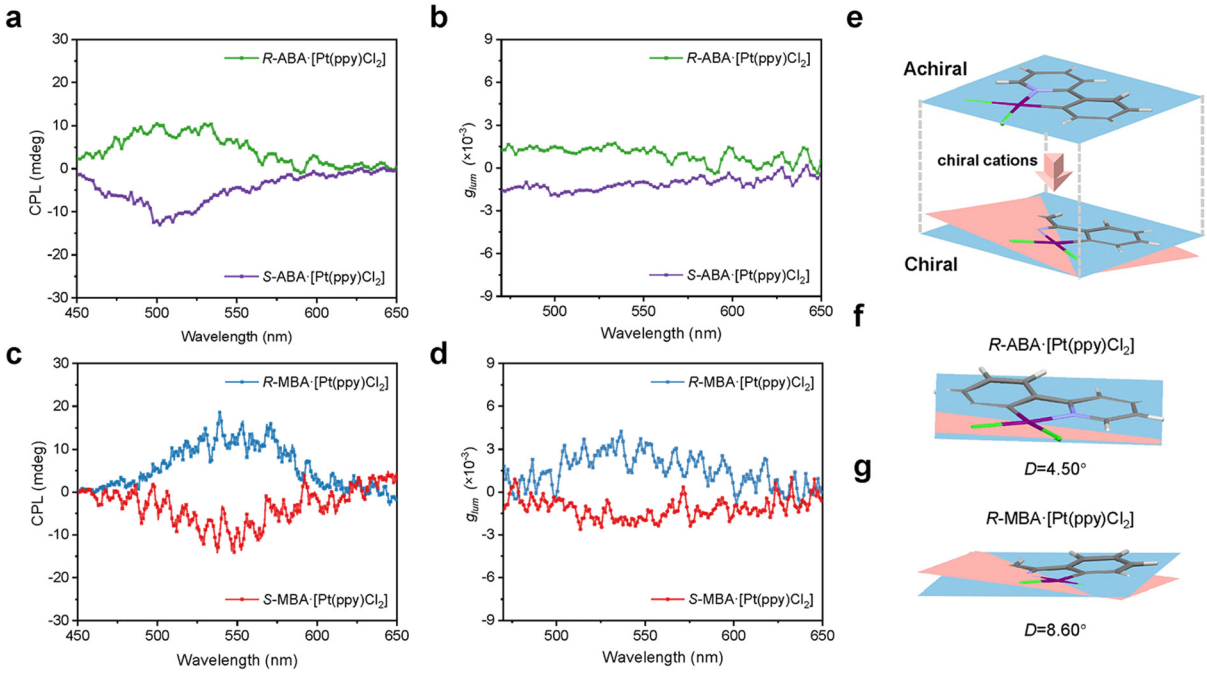

Fig. 7 CPL, g_{lum} spectra and chiral deformation of chiral Pt(II) complexes. (a) and (b) Measured CPL and corresponding g_{lum} spectra of *R*/*S*-ABA·[Pt(ppy)Cl$_2$]. (c) and (d) Measured CPL and corresponding g_{lum} spectra of *R*/*S*-MBA·[Pt(ppy)Cl$_2$]. (e) Dihedral angle (*D*) illustrations of the chiral cation-induced structural deformation for [Pt(ppy)Cl$_2$]$^-$. (f) and (g) The dihedral angles of [Pt(ppy)Cl$_2$]$^-$ at T_1 geometries for *R*-ABA·[Pt(ppy)Cl$_2$].

Table 2 Summary of the g_{lum}, electric transition dipole moment ($|\mu_e|$) and magnetic transition dipole moment ($|\mu_m|$) of the CPPL of *R*/*S*-ABA·[Pt(ppy)Cl$_2$] and *R*/*S*-MBA·[Pt(ppy)Cl$_2$]

	g_{lum}	$\lvert\mu_e\rvert$ [10^{-20} esu cm]	$\lvert\mu_m\rvert$ [10^{-20} erg G^{-1}]	$\lvert\mu_m\rvert/\lvert\mu_e\rvert$
R-ABA·[Pt(ppy)Cl$_2$]	$+1.4 \times 10^{-3}$	178.61	0.06	0.0004
S-ABA·[Pt(ppy)Cl$_2$]	-1.8×10^{-3}	175.69	0.08	0.0004
R-MBA·[Pt(ppy)Cl$_2$]	$+4.4 \times 10^{-3}$	214.29	0.24	0.0011
S-MBA·[Pt(ppy)Cl$_2$]	-2.8×10^{-3}	198.74	0.14	0.0007

R/*S*-ABA·[Pt(ppy)Cl$_2$] and *R*/*S*-MBA·[Pt(ppy)Cl$_2$] confirm that the luminescence center of [Pt(ppy)Cl$_2$]$^-$ is successfully induced by the chiral cations. The g_{abs} of *R*/*S*-ABA·[Pt(ppy)Cl$_2$] and *R*/*S*-MBA·[Pt(ppy)Cl$_2$] are $+1.1/-1.1 \times 10^{-4}$ and $+1.6/-2.0 \times 10^{-3}$, and the g_{lum} are $+1.4/-1.8 \times 10^{-3}$ for *R*/*S*-ABA·[Pt(ppy)Cl$_2$] and $+4.4/-2.8 \times 10^{-3}$ for *R*/*S*-MBA·[Pt(ppy)Cl$_2$], respectively. The stronger CD and CPL of *R*/*S*-MBA·[Pt(ppy)Cl$_2$] are attributed to its stronger chiral structural deformation and better matched electric and magnetic transition dipole moments. Our work expands the research field of circularly polarized phosphorescent materials and provides a new synthetic strategy to improve their chiroptical properties.

Author contributions

J. Ren performed the experimental synthesis and measurement, and wrote the draft. T. He performed the theoretical calculations and revised the paper. H. Lu, H. Wang, T. Shao, Z. Wang, Y. Zhang, S. Gull analysed the data. Y. Chi, Y. Zhong, Y. Chen and G. Long supervised; all the authors discussed the results and revised the manuscript.

Data availability

The data supporting this article have been included as part of the ESI.†

Conflicts of interest

There are no conflicts to declare.

Acknowledgements

The authors gratefully acknowledge the financial support from the NSFC (grant number: 92256202, 12261131500 and 52103218) of China, the Fundamental Research Funds for the Central Universities, Nankai University (grant number: 023-63223021) and the 111 Project (B18030).

References

1 H. Li, H. Li, W. Wang, Y. Tao, S. Wang, Q. Yang, Y. Jiang, C. Zheng, W. Huang and R. Chen, *Angew. Chem., Int. Ed.*, 2020, **59**, 4756–4762.
2 J. Han, S. Guo, H. Lu, S. Liu, Q. Zhao and W. Huang, *Adv. Opt. Mater.*, 2018, **6**, 1800538.
3 X. Wang, S. Ma, B. Zhao and J. Deng, *Adv. Funct. Mater.*, 2023, **33**, 2214364.

4 L. Gu, W. Ye, X. Liang, A. Lv, H. Ma, M. Singh, W. Jia, Z. Shen, Y. Guo, Y. Gao, H. Chen, D. Wang, Y. Wu, J. Liu, H. Wang, Y.-X. Zheng, Z. An, W. Huang and Y. Zhao, *J. Am. Chem. Soc.*, 2021, **143**, 18527–18535.
5 X. Wang, B. Zhao and J. Deng, *Adv. Mater.*, 2023, **35**, 2304405.
6 Z. Huang, Z. He, B. Ding, H. Tian and X. Ma, *Nat. Commun.*, 2022, **13**, 7841.
7 W. Chen, Z. Tian, Y. Li, Y. Jiang, M. Liu and P. Duan, *Chem. – Eur. J.*, 2018, **24**, 17444–17448.
8 S.-F. Wang, B.-K. Su, X.-Q. Wang, Y.-C. Wei, K.-H. Kuo, C.-H. Wang, S.-H. Liu, L.-S. Liao, W.-Y. Hung, L.-W. Fu, W.-T. Chuang, M. Qin, X. Lu, C. You, Y. Chi and P.-T. Chou, *Nat. Photonics*, 2022, **16**, 843–850.
9 S.-F. Wang, D.-Y. Zhou, K.-H. Kuo, C.-H. Wang, C.-M. Hung, J. Yan, L.-S. Liao, W.-Y. Hung, Y. Chi and P.-T. Chou, *Angew. Chem., Int. Ed.*, 2024, **63**, e202317571.
10 J. Song, H. Xiao, B. Zhang, L. Qu, X. Zhou, P. Hu, Z.-X. Xu and H. Xiang, *Angew. Chem., Int. Ed.*, 2023, **62**, e202302011.
11 G. Lu, Z.-G. Wu, R. Wu, X. Cao, L. Zhou, Y.-X. Zheng and C. Yang, *Adv. Funct. Mater.*, 2021, **31**, 2102898.
12 E. T. Luis, H. Iranmanesh, K. S. A. Arachchige, W. A. Donald, G. Quach, E. G. Moore and J. E. Beves, *Inorg. Chem.*, 2018, **57**, 8476–8486.
13 K. Tuong Ly, R.-W. Chen-Cheng, H.-W. Lin, Y.-J. Shiau, S.-H. Liu, P.-T. Chou, C.-S. Tsao, Y.-C. Huang and Y. Chi, *Nat. Photonics*, 2017, **11**, 63–68.
14 A. K.-W. Chan, M. Ng, Y.-C. Wong, M.-Y. Chan, W.-T. Wong and V. W.-W. Yam, *J. Am. Chem. Soc.*, 2017, **139**, 10750–10761.
15 Y. Yang, S. Xiao, Y. Zhou, C. Shi, L. Xu, X. Liao, N. Su, N. Sun, Y. Zheng, L. Ding and J. Ding, *Sci. China Mater.*, 2024, DOI: **10.1007/s40843-024-3042-1**.
16 Q. Ruan, Y. Cui, Z. Lin, X. Zhang, X. Zhang, Y. Li and X. Ma, *Sci. China Mater.*, 2024, **67**, 2302–2310.
17 C. Zhang, C. Ye, J. Yao and L. Wu, *Natl Sci. Rev.*, 2024, **11**, nwae244.
18 J. R. Brandt, X. Wang, Y. Yang, A. J. Campbell and M. J. Fuchter, *J. Am. Chem. Soc.*, 2016, **138**, 9743–9746.
19 J. Song, H. Xiao, L. Fang, L. Qu, X. Zhou, Z.-X. Xu, C. Yang and H. Xiang, *J. Am. Chem. Soc.*, 2022, **144**, 2233–2244.
20 M. Gon, R. Sawada, Y. Morisaki and Y. Chujo, *Macromolecules*, 2017, **50**, 1790–1802.
21 P. Fan, Z. Fang, S. Wang, Q. Dong, C. Xiao, A. J. McEllin, D. W. Bruce, W. Zhu and Y. Wang, *Chin. Chem. Lett.*, 2023, **34**, 107934.
22 Z. Jiang, J. Wang, T. Gao, J. Ma, Z. Liu and R. Chen, *ACS Appl. Mater. Interfaces*, 2020, **12**, 9520–9527.
23 T. Usuki, H. Uchida, K. Omoto, Y. Yamanoi, A. Yamada, M. Iwamura, K. Nozaki and H. Nishihara, *J. Org. Chem.*, 2019, **84**, 10749–10756.
24 J. Song, M. Wang, X. Xu, L. Qu, X. Zhou and H. Xiang, *Dalton Trans.*, 2019, **48**, 4420–4428.
25 Z.-Q. Li, Y.-D. Wang, J.-Y. Shao, Z. Zhou, Z.-L. Gong, C. Zhang, J. Yao and Y.-W. Zhong, *Angew. Chem., Int. Ed.*, 2023, **62**, e202302160.
26 Z.-Q. Li, Z.-L. Gong, T. Liang, S. Bernhard, Y.-W. Zhong and J. Yao, *Sci. China: Chem.*, 2023, **66**, 2892–2902.
27 G. Park, D. Y. Jeong, S. Y. Yu, J. J. Park, J. H. Kim, H. Yang and Y. You, *Angew. Chem., Int. Ed.*, 2023, **62**, e202309762.
28 Y.-J. Liu, Y. Liu and S.-Q. Zang, *Angew. Chem., Int. Ed.*, 2023, **62**, e202311572.
29 G. Long, R. Sabatini, M. I. Saidaminov, G. Lakhwani, A. Rasmita, X. Liu, E. H. Sargent and W. Gao, *Nat. Rev. Mater.*, 2020, **5**, 423–439.
30 Y. Xu, C. Li, Z. Li, J. Wang, J. Xue, Q. Wang, X. Cai and Y. Wang, *CCS Chem.*, 2022, **4**, 2065–2079.
31 X. Niu, Z. Zeng, Z. Wang, H. Lu, B. Sun, H.-L. Zhang, Y. Chen, Y. Du and G. Long, *Sci. China: Chem.*, 2024, **67**, 1961–1968.
32 L. Yan, M. K. Jana, P. C. Sercel, D. B. Mitzi and W. You, *J. Am. Chem. Soc.*, 2021, **143**, 18114–18120.
33 J.-T. Lin, D.-G. Chen, L.-S. Yang, T.-C. Lin, Y.-H. Liu, Y.-C. Chao, P.-T. Chou and C.-W. Chiu, *Angew. Chem., Int. Ed.*, 2021, **60**, 21434–21440.
34 H. Huang, Y. Yang, S. Qiao, X. Wu, Z. Chen, Y. Chao, K. Yang, W. Guo, Z. Luo, X. Song, Q. Chen, C. Yang, Y. Yu and Z. Zou, *Adv. Funct. Mater.*, 2024, **34**, 2309112.
35 G. Long, C. Jiang, R. Sabatini, Z. Yang, M. Wei, L. N. Quan, Q. Liang, A. Rasmita, M. Askerka, G. Walters, X. Gong, J. Xing, X. Wen, R. Quintero-Bermudez, H. Yuan, G. Xing, X. R. Wang, D. Song, O. Voznyy, M. Zhang, S. Hoogland, W. Gao, Q. Xiong and E. H. Sargent, *Nat. Photonics*, 2018, **12**, 528–533.
36 G. Fu, Y. He, W. Li, B. Wang, X. Lü, H. He and W.-Y. Wong, *J. Mater. Chem. C*, 2019, **7**, 13743–13747.
37 T. Ikeda, K. Hirano and T. Haino, *Mater. Chem. Front.*, 2018, **2**, 468–474.
38 E. V. Sokolova, M. A. Kinzhalov, A. S. Smirnov, A. M. Cheranyova, D. M. Ivanov, V. Y. Kukushkin and N. A. Bokach, *ACS Omega*, 2022, **7**, 34454–34462.
39 M. Ebina, A. Kobayashi, T. Ogawa, M. Yoshida and M. Kato, *Inorg. Chem.*, 2015, **54**, 8878–8880.
40 B. D. Belviso, F. Marin, S. Fuertes, V. Sicilia, R. Rizzi, F. Ciriaco, C. Cappuccino, E. Dooryhee, A. Falcicchio, L. Maini, A. Altomare and R. Caliandro, *Inorg. Chem.*, 2021, **60**, 6349–6366.
41 M. K. Jana, R. Song, H. Liu, D. R. Khanal, S. M. Janke, R. Zhao, C. Liu, Z. Valy Vardeny, V. Blum and D. B. Mitzi, *Nat. Commun.*, 2020, **11**, 4699.
42 H. Lu, T. He, H. Wu, F. Qi, H. Wang, B. Sun, T. Shao, T. Qiao, H.-L. Zhang, D. Sun, Y. Chen, Z. Tang and G. Long, *Adv. Funct. Mater.*, 2024, **34**, 2308862.
43 A. R. Lim, G. T. Schueneman and B. M. Novak, *Solid State Commun.*, 1999, **109**, 465–470.
44 X. Gong, O. Voznyy, A. Jain, W. Liu, R. Sabatini, Z. Piontkowski, G. Walters, G. Bappi, S. Nokhrin, O. Bushuyev, M. Yuan, R. Comin, D. McCamant, S. O. Kelley and E. H. Sargent, *Nat. Mater.*, 2018, **17**, 550–556.
45 O. Carugo, *Amino Acids*, 2018, **50**, 775–786.
46 L. Yao, G. Niu, J. Li, L. Gao, X. Luo, B. Xia, Y. Liu, P. Du, D. Li, C. Chen, Y. Zheng, Z. Xiao and J. Tang, *J. Phys. Chem. Lett.*, 2020, **11**, 1255–1260.

47 M. Maestri, D. Sandrini, V. Balzani, L. Chassot, P. Jolliet and A. von Zelewsky, *Chem. Phys. Lett.*, 1985, **122**, 375–379.
48 C. A. Craig, F. O. Garces, R. J. Watts, R. Palmans and A. J. Frank, *Coord. Chem. Rev.*, 1990, **97**, 193–208.
49 P.-I. Kvam, M. V. Puzyk, K. P. Balashev, J. Songstad, C. Lundberg, J. Arnarp, L. Björk and R. J. A. C. S. Gawinecki, *Acta Chem. Scand.*, 1995, **49**, 335–343.
50 M. Yoshida, V. Sääsk, D. Saito, N. Yoshimura, J. Takayama, S. Hiura, A. Murayama, K. Põhako-Esko, A. Kobayashi and M. Kato, *Adv. Opt. Mater.*, 2022, **10**, 2270028.
51 L. W. Chung, W. M. C. Sameera, R. Ramozzi, A. J. Page, M. Hatanaka, G. P. Petrova, T. V. Harris, X. Li, Z. Ke, F. Liu, H.-B. Li, L. Ding and K. Morokuma, *Chem. Rev.*, 2015, **115**, 5678–5796.
52 Y.-H. Zhou, A.-W. Zhang, R.-J. Huang, Y.-H. Sun, Z.-J. Chen, B.-S. Zhu and Y.-X. Zheng, *J. Mater. Chem. C*, 2023, **11**, 1329–1335.
53 X. Yang, X. Gao, Y.-X. Zheng, H. Kuang, C.-F. Chen, M. Liu, P. Duan and Z. Tang, *CCS Chem.*, 2023, **5**, 2760–2789.
54 T. He, M. Lin, H. Wang, Y. Zhang, H. Chen, C.-L. Sun, Z. Sun, X.-Y. Wang, H.-L. Zhang, Y. Chen and G. Long, *Adv. Theory Simul.*, 2024, **7**, 2300573.
55 M. Kobayashi, S. Masaoka and K. Sakai, *Photochem. Photobiol. Sci.*, 2009, **8**, 196–203.